RESEARCH ARTICLE

National Science Open
1: 20220014, 2022
https://doi.org/10.1360/nso/20220014

Earth and Environmental Sciences

Special Topic: Emerging Pollution and Emerging Pollutants

South-hemispheric marine aerosol Hg and S isotope compositions reveal different oxidation pathways

David AuYang[1,*], Jiubin Chen[2,1,*], Wang Zheng[2], Yanxu Zhang[3], Guitao Shi[4,5], Jeroen E. Sonke[6], Pierre Cartigny[7], Hongming Cai[2], Wei Yuan[2], Liangzhi Liu[8], Pengxue Gai[1] & Congqiang Liu[2]

[1]*State Key Laboratory of Environmental Geochemistry, Institute of Geochemistry, Chinese Academy of Sciences, Guiyang 550081, China;*
[2]*School of Earth System Science, Institute of Surface-Earth System Science, Tianjin University, Tianjin 300072, China;*
[3]*Joint International Research Laboratory of Atmospheric and Earth System Sciences, School of Atmospheric Sciences, Nanjing University, Nanjing 210023, China;*
[4]*Key Laboratory of Geographic Information Science (Ministry of Education), School of Geographic Sciences and State Key Lab of Estuarine and Coastal Research, East China Normal University, Shanghai 200241, China;*
[5]*Polar Research Institute of China, Shanghai 200062, China;*
[6]*Géosciences Environnement Toulouse, CNRS/IRD/Université Paul Sabatier Toulouse 3, Toulouse, France;*
[7]*Laboratoire de Géochimie des Isotopes Stables, Institut de Physique du Globe de Paris, Université Paris Diderot, CNRS UMR 7154, Sorbonne Paris-Cité, 1 rue de Jussieu, Paris 75005, France;*
[8]*School of Civil Engineering, Tianjin University, Tianjin 300072, China*

*Corresponding authors (emails: auyangdavid@gmail.com (David AuYang); jbchen@tju.edu.cn (Jiubin Chen))

Received 4 October 2021; Accepted 11 October 2021; Published online 15 April 2022

Abstract: Particle-bound mercury (PBM) records the oxidation of elemental mercury, of which the main oxidation pathways ($Br\cdot/Cl\cdot/OH\cdot/O_3$) remain unclear, especially in the Southern Hemisphere. Here, we present latitudinal covariations of Hg and S-isotopic anomalies in cross-hemispheric marine aerosols that evidence an equator-to-poleward transition of Hg oxidants from $OH\cdot/O_3$ in tropics to $Br\cdot/Cl\cdot$ in polar regions highlighting thus the presence of distinct oxidation processes producing PBM. The correlations between Hg, S and O-isotopic compositions measured in PBM, sulfates and nitrates respectively within the aerosols highlight the implication of common oxidants in their formations at different latitudes. Our results open a new window to better quantify the present-day atmospheric Hg, S and N budgets and to evaluate the influences of aerosols on climate and ecosystems once the isotopic fractionations associated with each process have been determined.

Keywords: mercury, sulfur, aerosols, oxidation, mass independent fractionation, marine

INTRODUCTION

Gaseous elemental mercury (GEM, Hg^0) is the main atmospheric Hg species, with a lifetime up to 1 year and can therefore be transported worldwide [1]. Hg^0 can be oxidized into gaseous oxidized mercury (GOM, Hg^{II}), a 10-day lifetime species which adsorbs readily on particles forming particle-bound Hg (PBM) [1]. Both gaseous and particulate Hg^{II} are transferred to terrestrial and marine ecosystems by rainfall and dry deposition. Upon deposition, Hg^{II} is partially transformed into methylmercury that can bioaccumulate in

aquatic organisms with well described impact on both wildlife and human health [2]. Both PBM and GOM concentrations controlled by complex atmospheric oxidation and reduction reactions, and the chemical forms (Hg^0, Hg^{II}) determine its atmospheric lifetime, deposition pathways and ecosystem loadings. However, many uncertainties persist in atmospheric mercury modeling, as the main atmospheric redox pathways of Hg remain unclear [3]. Identified oxidants include OH·, O_3, halogen species (mainly Br·) [4,5], and potentially NO_2· and HO_2· in a two-step oxidation mechanism initiated by Br· [6,7]. Atmospheric models based on either type of Hg^0 oxidants (i.e., OH·/O_3 or Br·) show good agreements with observed Hg^0 concentration and Hg^{II} wet deposition flux [6,8,9], but only after adjustment of terrestrial and marine Hg re-emissions. Recent computational and modeling studies suggest abundant photolysis of gaseous Hg-Br compounds back to Hg^0, thereby competing with Hg^{II} deposition [10,11]. Hg^{II} photolysis prolongs the atmospheric Hg lifetime up to 2 years, which is incompatible with observed Hg^0 variability in the planetary boundary layer [6,9], and suggests there are missing atmospheric oxidants. Atmospheric Hg redox mechanisms in global Hg transport and chemistry models are therefore ill-constrained, limiting our capacity for science-based Hg emission policy making.

Mercury stable isotopes could provide important information on the Hg^0 oxidation pathways because each of them should be associated with specific Hg-isotopic fractionations as demonstrated for halogen oxidants (e.g., Br·, Cl·) [12] and to be studied for some others including OH· and O_3. In particular, Hg isotopes show mass-independent fractionation (MIF) mainly caused by a variety of radical reactions during photochemical processes. MIF of odd Hg isotopes (odd Hg-MIF, Δ^{199}Hg and Δ^{201}Hg, see Methods) can be induced by magnetic isotope effects (MIE) or nuclear volume effects (NVE), with most odd-MIF observed in nature produced during aqueous and gas phase photochemical reactions and abiotic reduction of Hg^{II} [13–15]. MIF of even Hg isotopes (even Hg-MIF), leading to distinct Δ^{200}Hg and Δ^{204}Hg signatures, is not fully understood yet and has been suggested to occur during Hg photo-oxidation at the tropopause [16]. However, more recently, Sun *et al.* [12] suggested that the Hg^0 oxidation by halogen atoms (i.e., Br· and Cl·) would also produce both odd and even Hg-MIF, emphasizing the possible role of distinct Hg^0 oxidation pathway in the generation of MIF. Besides, significant insights into oxidative nitrate and sulfate formation, including quantifying the relative contributions of oxidants as OH·/O_3 or Br·/Cl·, i.e., the same as for Hg, have been made using sulfur (S) and/or oxygen (O) multiple isotopic compositions that also show MIF [17–20] (see Methods). For O-MIF, high values of Δ^{17}O in nitrate or sulfate up to 36‰ and 8‰ [21] result from the oxidation of NO_2 or SO_2 by H_2O_2 and O_3 which are characterized by a Δ^{17}O varying from 1.3‰ to 2.2‰ [20] and 20‰ to 35‰ [22–24], respectively, while oxidants like OH· in the troposphere, BrO and O_2+TMI produce sulfate with Δ^{17}O ~0‰ [19,25,26]. For S-MIF, the mechanisms suggested to be responsible for producing positive Δ^{33}S in modern aerosols are stratospheric sulfate inputs into the troposphere [27,28] and/or SO_2 oxidation by different oxidants (i.e., H_2O_2, O_3, OH·, O_2+TMI, BrO, etc.), while negative Δ^{33}S results from a mechanism related to combustion or heterogeneous reaction [17,18,29]. Despite the observation that PBM shows a significant relation with sulfate in aerosols [30] and shares similar oxidants (Supplementary Figure S1), S-Hg-O isotope systematics have never been coupled together to jointly understand the atmospheric oxidation budget and Hg redox cycling.

In this study, we target the Southern Hemisphere (SH) marine boundary layer, which provides an ideal place for studying atmospheric oxidation dynamics due to the absence of anthropogenic Hg and S point sources. We present new data for both Hg- (δ^{202}Hg, Δ^{199}Hg, Δ^{201}Hg, Δ^{200}Hg) and S- (δ^{34}S, Δ^{33}S and Δ^{36}S)

multiple isotopic compositions (see Methods) in marine aerosols collected shipboard during a cross-hemisphere round-trip cruise between Shanghai (China) and Antarctica (Figure 1, Supplementary Table S1). Coupled with O-isotopic compositions data from nitrate measured in the same set of samples [31], we show that the latitudinal isotopic gradients for Hg- and S-MIF in the SH indicate a shift in atmospheric oxidation pathway, and suggest that continental mineral dust plays an additional role in catalyzing Hg^0 and S oxidation.

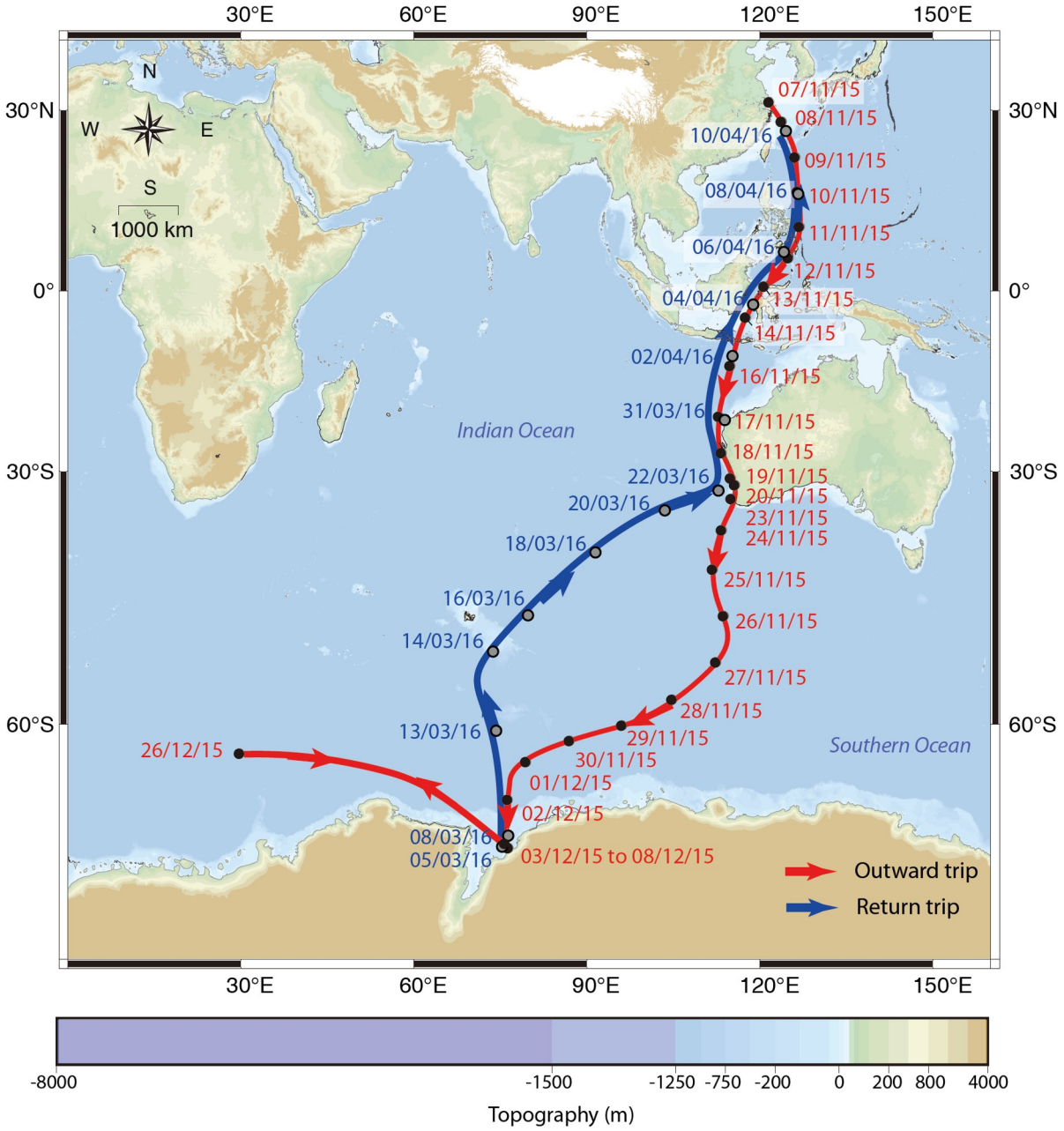

Figure 1 Map showing the sampling location during the round-trip cruise from November 2015 to April 2016.

RESULTS AND DISCUSSION

PBM samples are characterized by a δ^{202}Hg varying from −1.7‰ to 1.3‰ while δ^{34}S present a large variation ranging from −2.3‰ to 19.4‰. Δ^{199}Hg, Δ^{200}Hg and Δ^{201}Hg signatures varied from −0.74‰ to 0.54‰ (±0.02‰, 2σ), −0.06‰ to 0.33‰ (±0.04‰, 2σ) and −0.89‰ to 0.64‰ (±0.04‰, 2σ) respectively, while Δ^{33}S varied from 0.01‰ to 0.44‰ (±0.01‰, 2σ) during the entire cruise (Supplementary Table S2). A comparison of both Hg and S isotopic compositions (δ^{34}S, Δ^{33}S, Δ^{36}S and δ^{202}Hg, Δ^{199}Hg, Δ^{200}Hg and Δ^{201}Hg) with the literature data is presented in the Supplementary Information and Figures S2, S3.

Spatial variations exist between the subtropical Northern Hemisphere (st-NH i.e., 30° to 0°) and the SH, which may reflect different Hg oxidation pathways rather than natural and anthropogenic source contributions (see Supplementary Information S1.2). The SH is characterized by significant positive and monotonous Δ^{199}Hg, Δ^{200}Hg and Δ^{33}S latitudinal gradients from 70°S to 0° (*P*-value<0.01, 0.04 and <0.01, respectively, Figure 2), while no significant latitudinal gradient has been found in the (sub-)tropical NH (0° to 30°N) for neither Δ^{199}Hg, Δ^{200}Hg nor Δ^{33}S (*P*-value=0.91, 0.36, and 0.29, respectively). Moreover, several positive Δ^{33}S excursions up to 0.45‰ occur simultaneously with positive Δ^{200}Hg excursions up to 0.30‰ during the outward cruise off-shore West-Australia (08/11/15 to 25/11/15, white lines within the grey field of Figure 3), hereafter called “positive excursions period”.

During the positive excursions period, Δ^{33}S is significantly correlated to Δ^{200}Hg (*P*-value=0.04, Supplementary Figure S4c) but not to Δ^{199}Hg (*P*-value=0.43, Supplementary Figure S4a), possibly suggesting that a similar reaction/mechanism produces both Δ^{33}S and Δ^{200}Hg. We also observe that SH aerosol data deviate from the Δ^{200}Hg *vs*. Δ^{199}Hg slope of 3.4 defined by atmospheric Hg data (Supplementary Figure S5). At

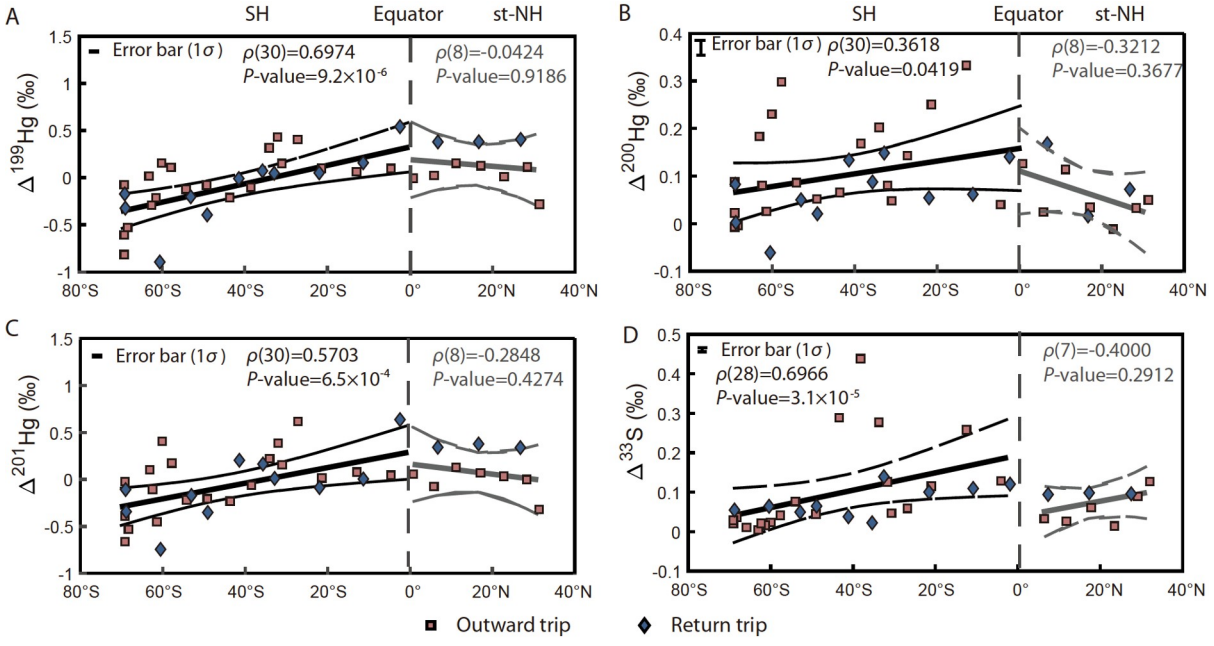

Figure 2 Variation of (A) Δ^{199}Hg, (B) Δ^{200}Hg, (C) Δ^{201}Hg, (D) Δ^{33}S during both outward and return (O/R) cruises as a function of latitude from the st-NH to the SH. A linear regression is applied for samples in the st-NH and SH. The Spearman correlation is reported by the ρ(df) notation for both st-NH and SH which include both O/R trip. df is the degree of freedom and the significance is reported by the *P*-value.

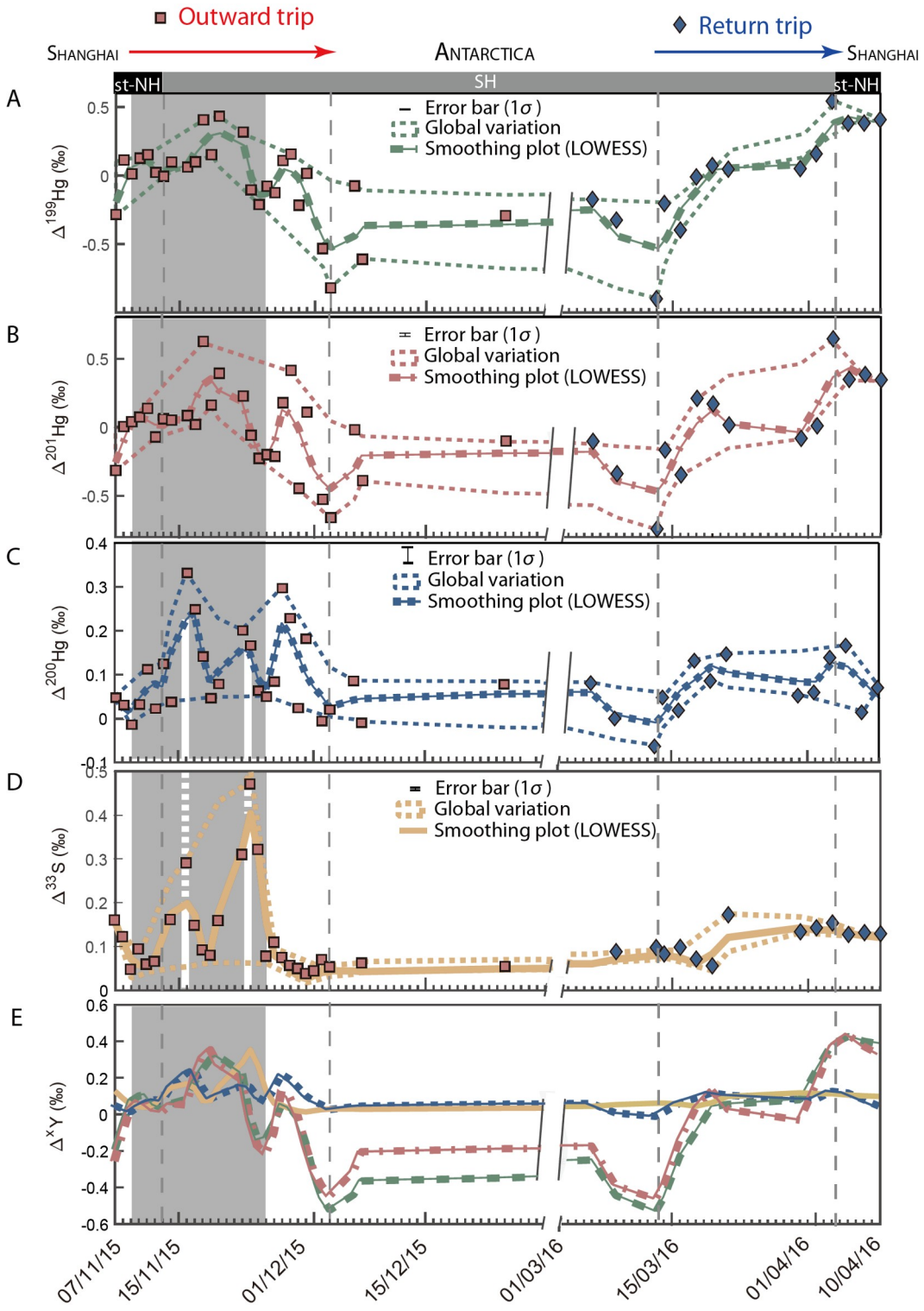

Figure 3 Variation of the (A) Δ^{199}Hg, (B) Δ^{201}Hg, (C) Δ^{200}Hg and (D) Δ^{33}S function of the sampling date. Smoothing plots (LOWESS) are also represented for each. (E) Compilation of the calculated smoothing plot function of the sampling date. Period with positive excursions highlighted with white strokes is represented by the grey rectangular.

present, no Hg mechanism at the Earth's surface is presently identified to generate Δ^{200}Hg shifts. Our data suggest, independently from Δ^{33}S, that we have detected production of Δ^{200}Hg in the marine boundary layer. During the remaining cruise period (26/11/15 to the end of the cruise 10/04/16), Δ^{33}S is significantly correlated to Δ^{199}Hg (*P*-value=0.02, Supplementary Figure S4b) but not to Δ^{200}Hg (*P*-value=0.93, Supplementary Figure S4d).

Thus, at least two reactions (and MIF-generating mechanisms) are involved: one responsible for both Hg-MIF (i.e., Δ^{199}Hg, Δ^{201}Hg, Δ^{200}Hg) and S-MIF (Δ^{33}S<0.20‰) latitudinal gradients in the SH and another responsible for the concomitant Δ^{33}S and Δ^{200}Hg positive excursions off-shore Western Australia.

Latitudinal S- and Hg-MIF gradients caused by shift in oxidants

The symmetric pattern observed during the outward and return (O/R) trips, 4 months apart, in Figures 2 and 3 suggests that positive latitudinal gradients of Hg-MIF and Δ^{33}S in the SH are a perennial feature. The gradients could result from a combination of control factors: a latitudinal isotope variability of Hg- and S-emissions, a relation with the solar incidence or/and a latitudinal variation in the oxidation pathways. Varying contributions of two or more Hg-sources with latitude are not consistent with known natural sources (see Supplementary Figures S6 and S7). In particular, anthropogenic Hg and S contributions are expected to remain relatively low, consistent with the generally low NO_3^- and SO_4^{2-} concentrations (except for the first three samples in the st-NH, see Supplementary Figure S8). Solar incidence also shows a latitudinal gradient suggesting a possible link to varying photochemical reactions. However, the solar insolation trends observed between November-December (outward trajectory) and March-April (return trajectory) in the Southern Hemisphere (0 to 90°S) are different with values varying from 450 to 500 W m^{-2} and 150 to 0 W m^{-2}, respectively [32], which would result in different intensity of photoreaction and thus different isotopic composition values. This is at odds with the similar Δ^{201}Hg values (and gradients) determined between the outward and return trips (i.e., y=0.0083x and y=0.0113x, at a threshold of α=0.05%, t=0.241<t(16, α)=2.120 using a Welch's *t*-test respectively) or with the Δ^{33}S values (and gradients) measured between the outward and return trips (i.e., y=0.0014x and y=0.0011x, at a threshold of α=0.05%, t=1.709<$t_{(16,\ \alpha)}$=2.120 using a Welch's *t*-test, respectively), ruling out the hypothesis. We suggest that in the SH marine boundary layer, the isotope signals of aerosol Hg and S may primarily be controlled by isotopic fractionation occurring during oxidation by oxidants such as O_3, OH· and halogen compounds (Br· and Cl·) in the marine boundary layer. These oxidants have been shown to be important for the oxidation of SO_2, species with a lifetime of ~2 days that result from the oxidation of DMS, the main S species emitted in the marine environment (up to 400 ppt *vs*. 200 ppt for SO_2) with a lifetime of 0.5 day [33], but also for Hg^0 [8,9], despite some theoretical doubts about the viability of O_3 and OH· [34].

A latitudinal change in oxidants is highlighted by the Δ^{200}Hg varying from values within the range reported for the experimental oxidation by Br· and Cl· [12] (i.e., 0.10‰ to 0.10‰) to values which cannot be explained yet (Δ^{200}Hg>0.10‰, Supplementary Figure S9), which we suggest might relate to an increase in the contribution of other oxidants in the Hg oxidation budget. Among the "other oxidants", OH· and O_3 are the most probable candidates as discussed above. Thus we will focus our discussion below on the possible role of OH· and O_3 in the Hg oxidation budget. However, we do not exclude the possibility that other unknown oxidants may also play a role. We use the GEOS-Chem atmospheric Hg chemistry and transport

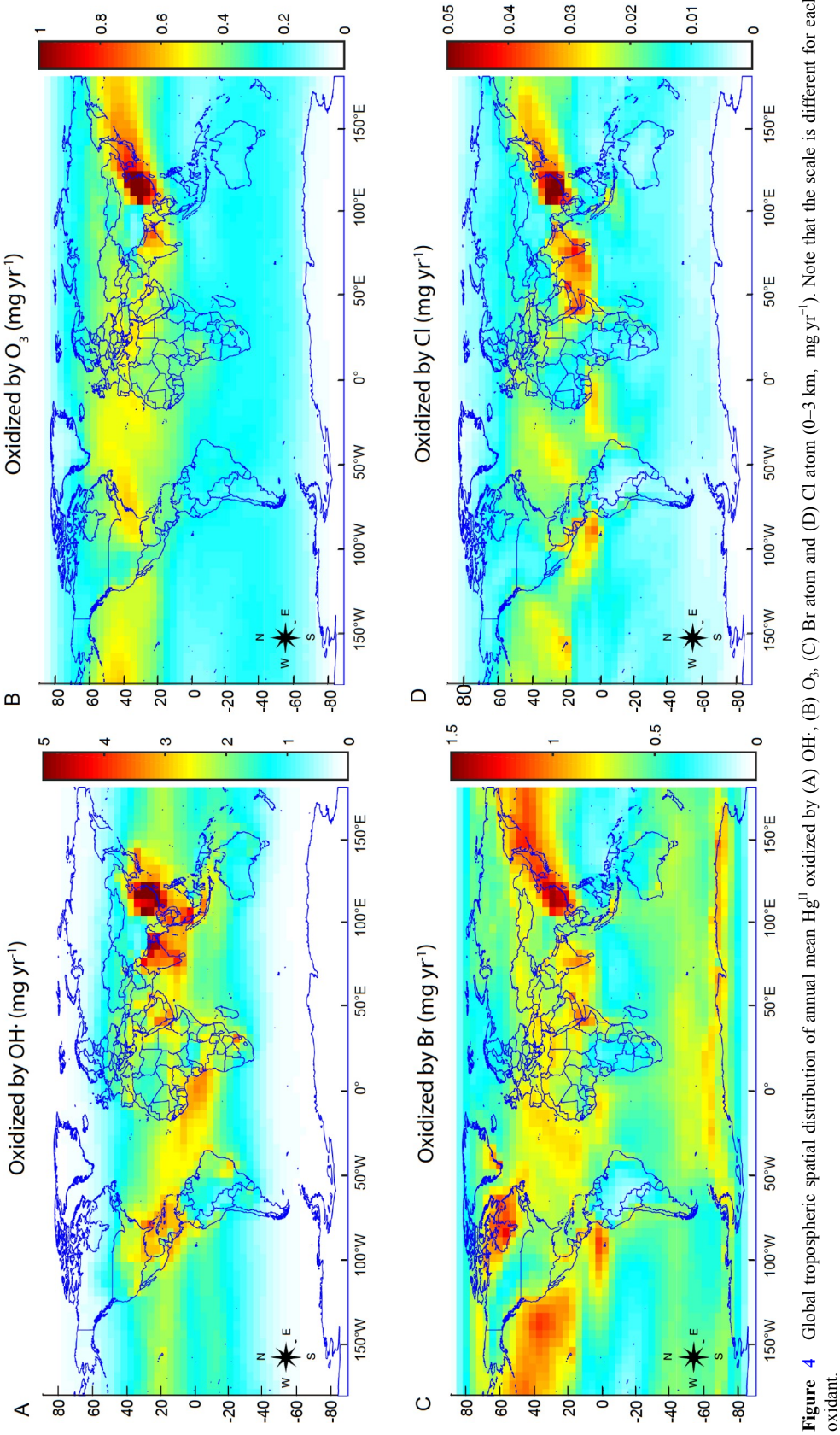

Figure 4 Global tropospheric spatial distribution of annual mean Hg^{II} oxidized by (A) OH·, (B) O_3, (C) Br atom and (D) Cl atom (0–3 km, mg yr^{-1}). Note that the scale is different for each oxidant.

model to estimate the annual, spatial contributions of four oxidants, OH·, O_3, Br·, and Cl·, to Hg^0 oxidation in the marine boundary layer and lower troposphere (0–3 km; see Methods). Our results show latitudinal variation of Hg^0 oxidation dominated by OH· and O_3 accounting for ~80% from 0 to 40°S, to an oxidation dominated by Br· accounting for ~75% of oxidation from 40°S to 80°S (Figure 4). Although the kinetic rate for the Hg^0 oxidation by O_3 estimated to be 10^{-19} and 10^{-20} cm^3/molecules [35,36] is the slowest among these oxidants [37,38], oxidation by O_3 needs to be considered given its relatively high concentrations compared with OH· or Br· (ppbv [39] *vs*. pptv [40] level, respectively), leading to significant amounts of Hg^{II} oxidized by O_3, i.e., maximum Hg^{II} produced by OH· and O_3 oxidation pathways of 5 and 1 mg yr^{-1}, respectively (Figure 4). Thus, the presence of different oxidation pathways could account for the Hg isotopic compositions and budget. This argument is in line with the recent study from Saiz-Lopez *et al.* [41], who proposed that at least one oxidation pathways responsible for the formation of PBM in the atmosphere is missing based on modeling study. It is however worth noting that aqueous photoreduction may also change the odd-MIF and thus could in theory explain the Δ^{199}Hg *vs*. Δ^{201}Hg slope of 0.93±0.1. However, photoreduction alone is unable to account for the variation of Δ^{200}Hg up to 0.20‰ measured during the remaining cruise period (that is not related to the Δ^{33}S from 26/11/15 to the end of the cruise 10/04/16), because photoreduction has not been shown to trigger any even-MIF as reported in previous studies [13,15]. Aqueous abiotic reduction of Hg^{II} can produce very small negative even-MIF in the remaining Hg(II) via NVE [42]. However, Δ^{200}Hg caused by NVE is proportional to δ^{202}Hg and is typically <0.10‰ unless δ^{202}Hg is unrealistically large (e.g., >10‰) [42]. Thus NVE cannot explain the up to 0.20‰ variation in Δ^{200}Hg.

For the S system, SO_4^{2-} production by progressive oxidation of marine DMS has typical values of δ^{34}S ~16‰ and Δ^{33}S ~0.05‰ [43]. Similar spatial distribution and variation of the annual mean concentration of gas-phase BrO, OH· and O_3 involved in DMS oxidation in the SH have been reported with oxidation dominated by OH·/O_3 up to 60% at latitude varying from 0° to 40°S to an oxidation dominated by BrO up to 70% at latitude varying from 40°S to 80°S [43]. Although S isotope fractionation associated with DMS oxidation to SO_2 has not been studied yet, the transition from dominant DMS oxidation by O_3/OH· to halogen compound is globally consistent with the GEOS-Chem results for Hg (Figure 4) [43]. Although measurement of O-MIF in sulfate from the same set of aerosols samples, which have been shown to be significantly correlated to the S-MIF in aerosols [28], would have brought additional information on the possible implication of different oxidation pathways, this data could not be obtained due to limited sample. However, the analyses of Δ^{17}O in NO_3 for the same set of samples in the SH [31] also show a latitudinal gradient with lower Δ^{17}O in the low latitudes and higher Δ^{17}O in polar region (Supplementary Figure S10, [31]), signing the transition from NO_2 oxidation by OH·/O_3 at the equator to oxidation by BrO near Antarctica [31]. Significant correlations between i) the Δ^{199}Hg with the Δ^{17}O ($\rho(26)$=−0.4132, *P*-value=0.03, Supplementary Figure S11a) and ii) Δ^{33}S with the Δ^{17}O ($\rho(26)$=−0.5050, *P*-value=0.01, Supplementary Figure S11b) suggest that these proxies (sulfate, nitrate and PBM) might be controlled by the same oxidants and that latitudinal oxidation gradient (pathways) for different species might be controlled by the concentration of different oxidants despite having distinct chemical reactions. Our data converge so that Hg^0 oxidation by OH·/O_3 might be a significant perennial process, dominant in the sub-tropics, and responsible for producing odd Hg-MIF, and possibly even Hg-MIF, with Δ^{200}Hg<0.20‰ observed in SH aerosols. Future experimental Hg isotope studies are required to demonstrate even Hg-MIF together with experimental DMS oxidation by

different oxidant to determine their isotopic fractionation.

Heterogeneous photoreactions on mineral dust might trigger even Hg-MIF

Super-imposed on the latitudinal gradients of both Hg- and S-MIF, which we attribute to the transition from $OH\cdot/O_3$ oxidation to halogen oxidation, are the positive Δ^{200}Hg and Δ^{33}S excursions of 0.30‰ and 0.40‰, respectively, that occur off-shore West-Australia (Figure 3). The restriction of these positive Δ^{33}S and Δ^{200}Hg excursions only during the outward trip highlights a sporadic mechanism. The mechanism triggering positive Δ^{200}Hg remains unclear [44], and significant insights could be gained from S-isotopes of the same samples. Both Δ^{200}Hg and Δ^{33}S are generally thought to be associated with stratospheric inputs [16,45,46] that have been reported intensively in this area, where stratospheric sulfate possibly reaches 1 μg m^{-3} [47]. Considering that the concentration of sulfate could reach 4 μg m^{-3} in our study, this could represent an injection of 25% of stratospheric sulfate in our samples, which could account for the highest Δ^{33}S of 0.44‰ considering that stratospheric sulfate would be characterized by a maximum Δ^{33}S of 10‰ [48]. However, this is inconsistent with our data which shows that samples characterized by both the highest Δ^{33}S up to 0.44‰ and Δ^{200}Hg up to 0.17‰ are composed of 90% of sea-salt sulfate (Supplementary Information). Moreover, if stratospheric injection were the sole mechanism responsible for the high Δ^{33}S and Δ^{200}Hg, high values of odd-MIF would also be expected due to the high contribution of photoreduction, which is not observed as these samples are characterized by low values of −0.07‰ and −0.10‰ for the odd-MIF. Furthermore, three-day HYSPLIT backward trajectory analysis for each sample, which is usually performed to discuss the S-MIF origin [45,49], shows that none originate from altitudes higher than 2000 m for initial trajectory release heights of 10 or 500 m, respectively (Supplementary Figure S12). Together with the fact that stratospheric-tropospheric mass flux exchanges are low in the tropics (30°N–30°S) with values varying from 0 to 20 kg s^{-1} km^{-2} [50] based on a lapse-rate tropopause method (comparatively, the highest mass flux is 600 kg s^{-1} km^{-2} in 30°N–60°N [50]), this again suggests that upper tropospheric or stratospheric Hg and S inputs would not be the sole mechanism responsible for the Δ^{200}Hg and Δ^{33}S excursions. To explain the S-MIF in sulfate aerosols varying from –0.60‰ to –0.50‰, photooxidation of SO_2 in the presence of mineral dust was recently suggested [29,51]. Although the implicated mechanism remains unconstrained yet, this hypothesis may account for both the higher SO_4^{2-} / Ca^{2+} enrichment factor used as a geochemical tracer for dust (see Supplementary Information) and the difference of Δ^{33}S between the O/R trip between Shanghai and Australia, as dust storms frequently occur from September to December in Australia [52]. The dust input hypothesis is consistent with i) the forward trajectories of dust particles concentration using HYSPLIT during this cruise which shows that dust particle paths may meet the sampling path only during the outward trip (Supplementary Figure S13); and ii) both positive Δ^{33}S and Δ^{36}S up to 0.44‰ and 1.21‰, respectively, measured in these samples that could only, to date, be explained by photooxidation [53] (Supplementary Figure S3). By analogy, we suggest that the occurrence of positive Δ^{200}Hg excursions up to 0.30‰ may also result from Hg^0 photo-oxidation catalyzed by mineral dust surfaces. This hypothesis is consistent with Chen *et al.* [16] who suggest that oxidation on aerosol surfaces could potentially promote the transformation of Hg^0 and produce positive Δ^{200}Hg. Although speculative, our findings suggest the possibility of even Hg-MIF produced at the Earth's surface, and should stimulate new experiments involving heterogeneous Hg transformations on aerosol and mineral surfaces to constrain the potential mechanisms.

Atmospheric Hg transformations over Antarctica

We observe negative Δ^{199}Hg and Δ^{201}Hg ranging from −0.50‰ to −0.30‰ during the ship's stay in Antarctica (Figure 3). These are associated with a strong increase in Hg concentration up to 140 pg m^{-3} (Supplementary Figure S8), while the concentration during the rest of the cruise is ~4 pg m^{-3}, consistent with literature data (2 to 8 pg m^{-3}) [54,55]. These variations are associated with variations in Δ^{200}Hg and Δ^{33}S close to 0‰ (from −0.01‰ to 0.08‰ and 0.00‰ to 0.06‰, respectively) highlighting again, other types of atmospheric Hg redox mechanisms. Aerosol Hg^{II} concentration peaks and negative odd Hg-MIF shift during the summer stay in Antarctica are unlikely to reflect higher Hg re-emission from seawater, since marine Hg is characterized by zero to positive Δ^{199}Hg up to 0.40‰ [43]. This is supported by the low Na^+ and Cl^- concentrations in these samples (Supplementary Figure S8) and HYSPLIT backward trajectories showing that the associated air masses are mainly stagnant over the Antarctic plateau (Supplementary Figure S12).

Instead, the Hg^{II} originally deposited on snow could be photoreduced into Hg^0, being later re-oxidized in the atmosphere and finally enriched on particles on the Antarctic plateau. Polar environments are unique with respect to the abundant photochemical release of Br from sea-ice and snow, which leads to intense Hg^0 oxidation especially during the springtime atmospheric mercury depletion event (AMDE) [5]. AMDEs occur both in the Arctic and Antarctica and deposit large amounts of Hg^{II} to surface snow, consistent with the intense Hg^0 oxidation reported on the Antarctic plateau [56,57] following the accumulation of oxidants within the shallow boundary layer during summer [57]. A significant fraction of deposited Hg^{II} in snowpack is then subsequently photoreduced and re-emitted back to the atmosphere [58]. This hypothesis is consistent with the fact that Hg^{II}-photoreduction in snow is associated with negative Δ^{199}Hg down to −5.50‰ in the residual Hg^{II} pool, which possibly could explain the initial negative Δ^{199}Hg (i.e., −0.50‰) measured in Antarctica aerosols. Moreover, successive oxidation and photoreduction could account for the Δ^{199}Hg shift observed from −0.50‰ to −0.30‰ in samples collected in Antarctica consistent with available evidence that photoreduction produces higher Δ^{199}Hg in Hg^0 and no change in Δ^{200}Hg [59] (Figure 3). Overall, these results are consistent with the known model of cyclical Hg oxidation and reduction in Antarctica during spring and summertime [60].

Implications for the oxidizing potential of the atmosphere

The latitudinal gradient of Hg isotope MIF in the aerosols collected along the cross-hemisphere cruise (30°N to 60°S) demonstrates that the two-step oxidation initiated by Br· cannot be the sole process responsible for Hg^0 oxidation in the SH marine boundary layer, emphasizing the need to consider additional oxidation pathways. This result is also consistent with the recent study from Saiz-Lopez *et al.* [41]. Modeled oxidation of S and Hg (also N) suggest an important shift in primary oxidants from the SH sub-tropics (OH·, O_3) to mid-latitudes and polar regions (Br·). Mass-independent signatures of S, O, and Hg isotopes in aerosols covary with the shift in oxidants, showing higher MIF in the subtropics which we relate to an increase in Hg oxidation by OH· and O_3. Previous global Hg modeling studies have opposed OH·, O_3 and Br as primary Hg oxidants [6,8,9]. Our study suggests independently from the model studies that both pathways operate in the different regions of the marine boundary layer and should be taken into account simultaneously, although future experimental isotopic studies need to be performed to support it and to quantitatively determine the

contribution of each oxidation pathway. We report additional S-MIF and even Hg-MIF signatures that might reflect the contribution of a reaction catalyzed by mineral dust emitted from the Australian continent. Heterogeneous oxidation chemistry on aerosol surfaces may provide the missing oxidation capacity observed in recent global atmospheric Hg models. Evidence for Hg^0 oxidation by $OH\cdot/O_3$ could be important in regions that are characterized by high concentrations of O_3 and might explain the positive relation between the Particles-Bound Mercury concentration and $PM_{2.5}$ concentration (i.e., mainly formed by physical and chemical processes in the atmosphere) observed in urban environment during pollution events [61]. These oxidation pathways reduce Hg^0 lifetime and increase Hg^{II} deposition rate locally, changing both Hg^{II} and Hg^0 fluxes. This ultimately leads to higher risk for human health as it would increase Hg^{II} deposition rate, for example, in tropical Asia (Figure 4) where fisheries catch dominates [62]. Further studies on combined MIF of O, S and Hg isotopes may also help understand a variety of scientific issues that could not be solved by single isotope system, such as the O-MIF of nitrate in Antarctica which remains debated [63,64], the origin of both sulfate and nitrate formed during polluted events in urban environment, and the evolution of Earth's atmosphere over geological times.

MATERIALS AND METHODS

Definition of MIF

The notation Δ is applied for both S and Hg isotopes as follows:

$$\Delta^{33}S = \delta^{33}S-((\delta^{34}S/1000+1)^{0.515}-1)\times1000$$

and

$$\Delta^{36}S = \delta^{36}S-((\delta^{34}S/1000+1)^{1.889}-1)\times1000$$

for the S isotopes and

$$\Delta^{199}Hg = \delta^{199}Hg-((\delta^{202}Hg/1000+1)^{0.252}-1)\times1000,$$

$$\Delta^{200}Hg = \delta^{200}Hg-((\delta^{202}Hg/1000+1)^{0.502}-1)\times1000$$

and

$$\Delta^{201}Hg = \delta^{201}Hg-((\delta^{202}Hg/1000+1)^{0.752}-1)\times1000$$

for the Hg isotopes.

Sample collection and processing

Aerosols were collected along the cruise track from Shanghai, China (31.32°N, 121.69°E) to East Antarctica (Zhongshan Station; 69.37°S, 76.37°E) during the 32nd Chinese Antarctic research expedition from November 2015 to April 2016. The aerosols were collected using a high volume air sampler (HVAS), which was placed on the top deck of the icebreaker RV *Xuelong*, about 25 m above the sea surface. The HVAS was controlled by wind direction and wind speed sensors, and it was operated only when the incoming wind was from a sector about 90° left and right on the ship's forward path, with the wind speed greater than 1.5 m s^{-1}, to avoid contamination of the ship emissions. The samples were collected on Whatman G653 glass-fiber filters (8×10in), which were prebaked at 550°C for 24 h and which have been used for both Hg, S and O isotopic

compositions [29,44,49,61,64–68]. Although this is the conventional sampling method for measuring the Hg isotopic compositions, several studies have shown that those methods lead to biases in PBM concentrations [69,70], underestimating their concentration. However, we argue that the MIF of PBM would not be significantly modified by these bias, because Hg MIF is primarily caused by photochemical processes. In general, the sampling durations were generally 24–72 h for each sample, with a flow rate of about 1.0 m^3 min^{-1}, thus leading to the sampling air volume of 1500–4000 m^3. In total, 42 aerosol samples were collected along the cruise path (Figure 1). All samples were kept in clean opaque polythene bags, preserved in insulated cabinets, and transported to China at –20°C.

In the laboratory, three quarters of each glass fiber filters were cut into pieces using pre-cleaned scissors that were rinsed between samples, placed in 100 mL Milli-Q water (18.2 MΩ), ultrasonicated for 40 min and leached for 24 h under shaking at 120 r min^{-1}. The extract solutions were then filtered through 0.22 μm PTFE filters for chemical ion concentration and isotopic composition (sulphate and nitrate) measurements. The remaining one quarter of filter was used for Hg isotope analysis.

Chemical analysis

Chemical ion concentration in sample solutions was determined using an ion chromatograph (ICS3000, Dionex, USA) following previous work [71]. In brief, the column used for cation analysis (Na^+, NH_4^+, K^+, Mg^{2+} and Ca^{2+}) was a Dionex column CS12 (2 mm×250 mm), with a guard column CG12 (2 mm×50 mm); while the anions (MSA, Cl^-, NO_3^- and SO_4^{2-}) were analyzed using a Dionex column AS11 (2 mm×250 mm) with a guard column AG11 (2 mm×50 mm). The eluents for cations and anions were MSA and potassium hydroxide (KOH), respectively. The relative standard deviation of ion concentrations in replicate samples (n=5) was generally <5%.

Concentrations of Hg were measured by a cold vapor atomic fluorescence spectroscopy (CVAFS, Tekran 2500) after reducing an aliquot of the pre-concentrated Hg^{II} into Hg^0 using $SnCl_2$. The Hg^0 is then collected on a gold-coated bead trap and analyzed [72].

S multi-isotope analysis

Part of the extracted solution was inserted into a reaction vessel heated at 180°C with 20 mL of Thode solution, a mixture of hydrochloric, hydroiodic and hypophosphorous acids [73], for 1.3 h to quantitatively reduce sulfate into H_2S. The formed gases were purged from the vessel using nitrogen gas, bubbled through deionized water and subsequently passed through a 0.3 mol L^{-1} silver nitrate ($AgNO_3$) solution to form silver sulfide (Ag_2S). This solid Ag_2S was then rinsed twice with Millipore water and dried at 70°C overnight. Ag_2S was then loaded into an aluminum foil, weighted and degassed under vacuum.

Ag_2S was subsequently converted to SF_6 by reacting with approximately 200 Torr of excess fluorine in a nickel bomb at 250°C (1 Torr=1.333×10^2 Pa). The produced SF_6 was purified using both cryogenic techniques and gas chromatography, quantified and subsequently analyzed by dual inlet isotope ratio mass spectrometry (Thermo-Fisher MAT-253) where m/z=127, 128, 129 and 131 ion beams were monitored.

The $\delta^{34}S$-values were measured against our in-house SF_6 tank that had been previously calibrated with respect to the IAEA-S1 international standards and expressed versus V-CDT assuming a $\delta^{34}S_{S1}$=−0.3‰ *vs*. V-

CDT isotope composition. To express our $\Delta^{33}S$ and $\Delta^{36}S$ data with respect to V-CDT, we anchored our data using CDT-data measured previously in the laboratory following Defouilloy *et al.* [74]. No further corrections were carried out, other than normalization of the data to CDT. $\Delta^{33}S$ and $\Delta^{36}S$ IAEA-standards were within values reported elsewhere [74–76]. Our analysis (n=5) of IAEA-S1 standard yielded: $\delta^{34}S$=−0.33‰ ±0.02‰, $\Delta^{33}S$=0.074‰±0.010‰ and $\Delta^{36}S$=−0.809‰±0.128‰ *vs*. CDT. Analyses of the international sulfate standard NBS-127 was also performed and gave a $\delta^{34}S$ of 20.8‰±0.4‰ (2σ; n=12), consistent with the 20.3‰±0.4‰ value reported by the IAEA. Field blank samples (n=2) were analyzed and generated no sulfate when we followed the chemistry method described below.

Hg multi-isotope analysis

The remaining 1/4 filters have been combusted using a dual stage combustion protocol to pre-concentrate the Hg. This protocol is detailed in Huang *et al.* [72]. Briefly, the filter is introduced in a quartz tube, and inserted in the first tube furnace, which rapidly ramps the temperature to 950°C for 3.5 h, while the second furnace is maintained at a constant temperature of 1000°C to pyrolize all combustion products to CO_2, H_2O, SO_2, and Hg^0 [77]. The combustion products are purged by Hg-free O_2 and bubbled in a 5 mL acid trap consisting of a mixture of HNO_3, HCl and water (2:4:9) [72,77]. The acid trapping solution is then transferred to a pre-cleaned glass bottle, diluted with milli-Q water and 50 µL of 0.2 mol L^{-1} BrCl.

Pre-concentrated, purified Hg^{II} samples were then converted to Hg^0 after reaction with $SnCl_2$ and injected in a multi-collector inductively coupled plasma mass spectrometer (Neptune plus), simultaneously with Tl as an internal standard to correct instrumental mass bias [78,79]. High concentration of Tl (20 ppb, 1 ppb= µg L^{-1}) is injected to prevent the formation of Hg hydrides [78] during the analysis. The faraday cups were positioned to collect ^{198}Hg (L3), ^{199}Hg (L2), ^{200}Hg (L1), ^{201}Hg (C), ^{202}Hg (H1), ^{203}Tl (H2) and ^{205}Tl (H3). ^{196}Hg and ^{204}Hg were not analyzed. Hg isotopic composition is then calculated using the bracketed Hg standard NIST 3133. Varying concentrations of the international standard NIST 3177 from 2 to 0.25 ppb to match the samples concentration were also regularly analyzed to test the stability of the Neptune plus (i.e., secondary standard solutions) [80]. Analyses of the NIST 3177 (UM-Almaden) over the analyses session for 0.25 ppb (n=6) gave $\delta^{202}Hg$=−0.53‰±0.03‰ (2σ), $\Delta^{199}Hg$=−0.04‰±0.08‰ (2σ), $\Delta^{200}Hg$=−0.01‰±0.06‰ (2σ), $\Delta^{201}Hg$=−0.01‰±0.05‰ (2σ) *vs*. NIST 3133. Analyses of the NIST 3177 over the session for 0.5 ppb (n=12) gave $\delta^{202}Hg$=−0.55‰±0.04‰ (2σ), $\Delta^{199}Hg$=−0.01‰±0.08‰ (2σ), $\Delta^{200}Hg$=0.00‰±0.04‰ (2σ), $\Delta^{201}Hg$= 0.01‰±0.05‰ (2σ) *vs*. NIST 3133. Analyses of the NIST 3177 over the session for 2 ppb (n=16) gave $\delta^{202}Hg$=−0.52‰±0.03‰ (2σ), $\Delta^{199}Hg$=−0.03‰±0.04‰ (2σ), $\Delta^{200}Hg$=0.00‰±0.03‰ (2σ), $\Delta^{201}Hg$=−0.01‰ ±0.02‰ (2σ) *vs*. NIST 3133. All repeated analyses of 3177 are consistent with previous reported values [12,44,81–84].

Analysis of the certified reference material CRM024 (n=6), a Chinese loamy sand characterized by 0.71 ppm of Hg (1 ppm=1 mg L^{-1}), gave $\delta^{202}Hg$=−1.43‰±0.08‰ (2σ), $\Delta^{199}Hg$=0.032‰±0.019‰ (2σ), $\Delta^{200}Hg$=−0.001‰±0.023‰ (2σ), $\Delta^{201}Hg$=0.003‰±0.012‰ (2σ) *vs*. NIST 313 and a recovery of 102%±5% after the preconcentration protocol by dual-stage combustion, consistent with the values reported previously [72]. Field blank samples (n=2) have also been analyzed and showed concentrations of Hg under the analytical detection limit (<0.1 ppb).

LOWESS and statistics

The LOWESS smoothing has been calculated by MATLAB using a linear polynomial function with a span of 25%.

In the following, the significance of each correlation is calculated using a Spearman Correlation as this non-parametrical test does not carry any assumption about the data distribution and is not sensitive to outliers.

Hysplit analysis

To investigate relationships between the origins of the air masses and the isotopic compositions of S and Hg measured in marine aerosols, 72 h backward trajectories at 10 and 500 m height have been modeled using HYSPLIT—Hybrid Single Particles Lagrangian Integrated Trajectory—for each sample. The model used NCEP-NCAR reanalysis data fields with a resolution of 0.5×0.5. Backward trajectories for the samples are then incorporated into a map generated by generic mapping tools. Global Relief data come from ETOPO2 (last access: 06/05/19) [85]. In addition, 72 h foreward trajectories for dust emission sources have been modeled using HYSPLIT. Coordinates of Australian deserts were compiled from the NOAA and Natural Earth (last access: 06/05/19 https://www.arl.noaa.gov/hysplit/dust/ and https://www.naturalearthdata.com/downloads/). The simulation considered an arbitrary particle released by cycle of 100 and an emission rate of 61Tg/year [86]).

GEOS-Chem simulation

We use a global three-dimensional atmospheric chemistry and transport model GEOS-Chem (version 12.1.0) to simulate the Hg redox chemistry (www.geos-chem.org) following Horowitz *et al.* [6]. It has a horizontal resolution of 4° latitude ×5° longitude with 47 vertical layers. The model is driven by GEOS-FP assimilated meteorological data from the NASA Global Modeling and Assimilation Office. The anthropogenic emissions are from Zhang *et al.* [87] with land and ocean re-emissions from Selin *et al.* [88] and Zhang *et al.* [89]. The model induces Hg redox chemistry summarized by Horowitz *et al.* [6], in which Hg^0 is oxidized to Hg^{II} in a two-stage process including an initial oxidation by halogen atoms (Br and Cl) and secondary oxidation by Br, Cl, HO_2, OH, NO_2, ClO and BrO. In addition, we include the oxidation of Hg^0 by OH and O_3 following Selin *et al.* [88]. The reduction of Hg^{II} to Hg^0 is simulated as photolysis of aqueous-phase Hg^{II}-organic complexes in aerosols and clouds. The gas-particle partitioning between Hg^{II} and Hg_p is simulated as a thermodynamic equilibrium function of local temperature and fine particulate matter concentrations ($PM_{2.5}$) following Amos *et al.* [90]. The model is run for 2014–2016 with the result of first year discarded as spin-up time.

Data availability

The data supporting the findings of this study are available within the article and its Supplementary Information files. Data analysis codes include MATLAB built-in functions and GEOS-Chem simulation as described in the Method section.

Funding

This study was supported by the National Natural Science Foundation of China (41830647, 41625012, 41961144028,

U1612442) to JB.C and the Chinese Academy of Science President's International Fellowship Initiative PIFI-C (2018PC0034) to D.AY.

Author contributions

D.AY., JB.C and GT.S designed the study. D.AY. performed both S-isotopic composition analysis and the Hg-isotopic composition analysis with contribution from PX.G. YX.Z performed the GEOS-Chem model. GT.S collected the aerosols, processed the samples, performed the chemical analysis and performed the O-isotopic compositions used in the discussion. D. AY wrote the manuscript with JB.C, JE.S, W.Z, P.C and contributions from all coauthors. All authors read and commented on the manuscript.

Conflict of interest

The authors declare that they have no conflict of interest.

Supplementary information

The supporting information is available online at https://doi.org/10.1360/nso/20220014. The supporting materials are published as submitted, without typesetting or editing. The responsibility for scientific accuracy and content remains entirely with the authors.

References

1 Selin NE. Global biogeochemical cycling of mercury: a review. *Annu Rev Environ Resour* 2009; **34**: 43–63.
2 Global Mercury Assessment 2018. United Nations Environment Programme, Chemicals and Health Branch Geneva. 2019.
3 Si L, Ariya P. Recent advances in atmospheric chemistry of mercury. *Atmosphere* 2018; **9**: 76.
4 Steffen A, Douglas T, Amyot M, *et al.* A synthesis of atmospheric mercury depletion event chemistry in the atmosphere and snow. *Atmos Chem Phys* 2008; **8**: 1445–1482.
5 Temme C, Einax JW, Ebinghaus R, *et al.* Measurements of atmospheric mercury species at a coastal site in the antarctic and over the South Atlantic Ocean during Polar Summer. *Environ Sci Technol* 2003; **37**: 22–31.
6 Horowitz HM, Jacob DJ, Zhang Y, *et al.* A new mechanism for atmospheric mercury redox chemistry: implications for the global mercury budget. *Atmos Chem Phys* 2017; **17**: 6353–6371.
7 Wang F, Saiz-Lopez A, Mahajan AS, *et al.* Enhanced production of oxidised mercury over the tropical Pacific Ocean: a key missing oxidation pathway. *Atmos Chem Phys* 2014; **14**: 1323–1335.
8 De Simone F, Cinnirella S, Gencarelli CN, *et al.* Model study of global mercury deposition from biomass burning. *Environ Sci Technol* 2015; **49**: 6712–6721.
9 Travnikov O, Angot H, Artaxo P, *et al.* Multi-model study of mercury dispersion in the atmosphere: atmospheric processes and model evaluation. *Atmos Chem Phys* 2017; **17**: 5271–5295.
10 Saiz-Lopez A, Acuña AU, Trabelsi T, *et al.* Gas-phase photolysis of Hg(I) radical species: a new atmospheric mercury reduction process. *J Am Chem Soc* 2019; **141**: 8698–8702.
11 Saiz-Lopez A, Sitkiewicz SP, Roca-Sanjuán D, *et al.* Photoreduction of gaseous oxidized mercury changes global atmospheric mercury speciation, transport and deposition. *Nat Commun* 2018; **9**: 4796.
12 Sun G, Sommar J, Feng X, *et al.* Mass-dependent and-independent fractionation of mercury isotope during gas-phase oxidation of elemental mercury vapor by atomic Cl and Br. *Environ Sci Technol* 2016; **50**: 9232–9241.
13 Bergquist BA, Blum JD. Mass-dependent and-independent fractionation of Hg isotopes by photoreduction in aquatic systems. *Science* 2007; **318**: 417–420.
14 Estrade N, Carignan J, Sonke JE, *et al.* Mercury isotope fractionation during liquid-vapor evaporation experiments.

Geochim Cosmochim Acta 2009; **73**: 2693–2711.

15 Zheng W, Hintelmann H. Mercury isotope fractionation during photoreduction in natural water is controlled by its Hg/DOC ratio. *Geochim Cosmochim Acta* 2009; **73**: 6704–6715.

16 Chen JB, Hintelmann H, Feng XB, *et al.* Unusual fractionation of both odd and even mercury isotopes in precipitation from Peterborough, ON, Canada. *Geochim Cosmochim Acta* 2012; **90**: 33–46.

17 Au Yang D, Bardoux G, Assayag N, *et al.* Atmospheric SO_2 oxidation by NO_2 plays no role in the mass independent sulfur isotope fractionation of urban aerosols. *Atmos Environ* 2018; **193**: 109–117.

18 Harris E, Sinha B, Hoppe P, *et al.* High-precision measurements of ^{33}S and ^{34}S fractionation during SO_2 oxidation reveal causes of seasonality in SO_2 and sulfate isotopic composition. *Environ Sci Technol* 2013; **47**: 12174–12183.

19 Lyons JR. Transfer of mass-independent fractionation in ozone to other oxygen-containing radicals in the atmosphere. *Geophys Res Lett* 2001; **28**: 3231–3234.

20 Savarino J, Thiemens MH. Analytical procedure to determine both $\delta^{18}O$ and $\delta^{17}O$ of H_2O_2 in natural water and first measurements. *Atmos Environ* 1999; **33**: 3683–3690.

21 Savarino J, Lee CCW, Thiemens MH. Laboratory oxygen isotopic study of sulfur (IV) oxidation: origin of the mass-independent oxygen isotopic anomaly in atmospheric sulfates and sulfate mineral deposits on Earth. *J Geophys Res* 2000; **105**: 29079–29088.

22 Krankowsky D, Bartecki F, Klees GG, *et al.* Measurement of heavy isotope enrichment in tropospheric ozone. *Geophys Res Lett* 1995; **22**: 1713–1716.

23 Johnston JC, Thiemens MH. The isotopic composition of tropospheric ozone in three environments. *J Geophys Res* 1997; **102**: 25395–25404.

24 Vicars WC, Savarino J. Quantitative constraints on the ^{17}O-excess ($\Delta^{17}O$) signature of surface ozone: Ambient measurements from 50°N to 50°S using the nitrite-coated filter technique. *Geochim Cosmochim Acta* 2014; **135**: 270–287.

25 Holt BD, Cunningham PT, Kumar R. Oxygen isotopy of atmospheric sulfates. *Environ Sci Technol* 1981; **15**: 804–808.

26 Barkan E, Luz B. High precision measurements of $^{17}O/^{16}O$ and $^{18}O/^{16}O$ ratios in H_2O. *Rapid Commun Mass Spectrom* 2005; **19**: 3737–3742.

27 Lin M, Kang S, Shaheen R, *et al.* Atmospheric sulfur isotopic anomalies recorded at Mt. Everest across the Anthropocene. *Proc Natl Acad Sci USA* 2018; **115**: 6964–6969.

28 Romero AB, Thiemens MH. Mass-independent sulfur isotopic compositions in present-day sulfate aerosols. *J Geophys Res-Atmos* 2003; **108**.

29 Au Yang D, Cartigny P, Desboeufs K, *et al.* Seasonality in the $\Delta^{33}S$ measured in urban aerosols highlights an additional oxidation pathway for atmospheric SO_2. *Atmos Chem Phys* 2019; **19**: 3779–3796.

30 Chen X, Balasubramanian R, Zhu Q, *et al.* Characteristics of atmospheric particulate mercury in size-fractionated particles during haze days in Shanghai. *Atmos Environ* 2016; **131**: 400–408.

31 Shi G, Ma H, Zhu Z, *et al.* Using stable isotopes to distinguish atmospheric nitrate production and its contribution to the surface ocean across hemispheres. *Earth Planet Sci Lett* 2021; **564**: 116914.

32 Berger A, Yin Q. Chapter 15—Modelling the past and future interglacials in response to astronomical and greenhouse gas forcing. In: Henderson-Sellers A, Mcguffie K, eds. *The Future of the World's Climate (2nd ed)*. Boston: Elsevier. 2012: 437–462.

33 Seinfeld JH, Pandis SN. Atmospheric Chemistry and Physics: From Air Pollution to Climate Change. Hoboken: John Wiley & Sons, 2012.

34 Calvert JG, Lindberg SE. Mechanisms of mercury removal by O and OH in the atmosphere. *Atmos Environ* 2005; **39**: 3355–3367.

35 Hall B. The gas phase oxidation of elemental mercury by ozone. *Water Air Soil Pollut* 1995; **80**: 301–315.

36 Pal B, Ariya PA. Studies of ozone initiated reactions of gaseous mercury: kinetics, product studies, and atmospheric implications. *Phys Chem Chem Phys* 2004; **6**: 572.

37 Raofie F, Ariya PA. Product study of the gas-phase BrO-initiated oxidation of Hg^0: evidence for stable Hg^{1+} compounds. *Environ Sci Technol* 2004; **38**: 4319–4326.

38 Sommar J, Gårdfeldt K, Strömberg D, *et al.* A kinetic study of the gas-phase reaction between the hydroxyl radical and atomic mercury. *Atmos Environ* 2001; **35**: 3049–3054.

39 Lu X, Zhang L, Zhao Y, *et al.* Surface and tropospheric ozone trends in the Southern Hemisphere since 1990: possible linkages to poleward expansion of the Hadley Circulation. *Sci Bull* 2019; **64**: 400–409.

40 Stone D, Whalley LK, Heard DE. Tropospheric OH and HO_2 radicals: field measurements and model comparisons. *Chem Soc Rev* 2012; **41**: 6348.

41 Saiz-Lopez A, Travnikov O, Sonke JE, *et al.* Photochemistry of oxidized Hg(I) and Hg(II) species suggests missing mercury oxidation in the troposphere. *Proc Natl Acad Sci USA* 2020; **117**: 30949–30956.

42 Yang S, Liu Y. Nuclear volume effects in equilibrium stable isotope fractionations of mercury, thallium and lead. *Sci Rep* 2015; **5**: 12626.

43 Chen Q, Sherwen T, Evans M, *et al.* DMS oxidation and sulfur aerosol formation in the marine troposphere: a focus on reactive halogen and multiphase chemistry. *Atmos Chem Phys* 2018; **18**: 13617–13637.

44 Fu X, Zhang H, Feng X, *et al.* Domestic and transboundary sources of atmospheric particulate bound mercury in remote areas of China: evidence from mercury isotopes. *Environ Sci Technol* 2019; **53**: 1947–1957.

45 Guo Z, Li Z, Farquhar J, *et al.* Identification of sources and formation processes of atmospheric sulfate by sulfur isotope and scanning electron microscope measurements. *J Geophys Res* 2010; **115**: D00K07.

46 Lin M, Zhang Z, Su L, *et al.* Unexpected high ^{35}S concentration revealing strong downward transport of stratospheric air during the monsoon transitional period in East Asia. *Geophys Res Lett* 2016; **43**: 2315–2322.

47 Kleinschmitt C, Boucher O, Platt U. Sensitivity of the radiative forcing by stratospheric sulfur geoengineering to the amount and strategy of the SO_2 injection studied with the LMDZ-S3A model. *Atmos Chem Phys* 2018; **18**: 2769–2786.

48 Ono S, Whitehill AR, Lyons JR. Contribution of isotopologue self-shielding to sulfur mass-independent fractionation during sulfur dioxide photolysis. *J Geophys Res-Atmos* 2013; **118**: 2444–2454.

49 Han X, Guo Q, Strauss H, *et al.* Multiple sulfur isotope constraints on sources and formation processes of sulfate in Beijing $PM_{2.5}$ aerosol. *Environ Sci Technol* 2017; **51**: 7794–7803.

50 Boothe AC, Homeyer CR. Global large-scale stratosphere-troposphere exchange in modern reanalyses. *Atmos Chem Phys* 2017; **17**: 5537–5559.

51 Genot I, Au Yang D, Martin E, *et al.* Oxygen and sulfur mass-independent isotopic signatures in black crusts: the complementary negative $\Delta^{33}S$ reservoir of sulfate aerosols? *Atmos Chem Phys* 2020; **20**: 4255–4273.

52 McGowan H, Clark A. Identification of dust transport pathways from Lake Eyre, Australia using Hysplit. *Atmos Environ* 2008; **42**: 6915–6925.

53 Whitehill AR, Ono S. Excitation band dependence of sulfur isotope mass-independent fractionation during photochemistry of sulfur dioxide using broadband light sources. *Geochim Cosmochim Acta* 2012; **94**: 238–253.

54 Nerentorp Mastromonaco M, Gårdfeldt K, Jourdain B, *et al.* Antarctic winter mercury and ozone depletion events over sea ice. *Atmos Environ* 2016; **129**: 125–132.

55 Spolaor A, Angot H, Roman M, *et al.* Feedback mechanisms between snow and atmospheric mercury: results and observations from field campaigns on the Antarctic Plateau. *Chemosphere* 2018; **197**: 306–317.

56 Dommergue A, Barret M, Courteaud J, *et al.* Dynamic recycling of gaseous elemental mercury in the boundary layer of the Antarctic Plateau. *Atmos Chem Phys* 2012; **12**: 11027–11036.

57 Angot H, Magand O, Helmig D, *et al.* New insights into the atmospheric mercury cycling in central Antarctica and implications on a continental scale. *Atmos Chem Phys* 2016; **16**: 8249–8264.

58 Kirk JL, St. Louis VL, Sharp MJ. Rapid reduction and reemission of mercury deposited into snowpacks during atmospheric mercury depletion events at Churchill, Manitoba, Canada. *Environ Sci Technol* 2006; **40**: 7590–7596.

59 Sherman LS, Blum JD, Johnson KP, *et al.* Mass-independent fractionation of mercury isotopes in Arctic snow driven by sunlight. *Nat Geosci* 2010; **3**: 173–177.

60 Song S, Angot H, Selin NE, *et al.* Understanding mercury oxidation and air-snow exchange on the East Antarctic Plateau: a modeling study. *Atmos Chem Phys* 2018; **18**: 15825–15840.

61 Huang Q, Chen J, Huang W, *et al.* Isotopic composition for source identification of mercury in atmospheric fine particles. *Atmos Chem Phys* 2016; **16**: 11773–11786.

62 Watson RA. A database of global marine commercial, small-scale, illegal and unreported fisheries catch 1950–2014. *Sci Data* 2017; **4**: 170039.

63 Savarino J, Kaiser J, Morin S, *et al.* Nitrogen and oxygen isotopic constraints on the origin of atmospheric nitrate in coastal Antarctica. *Atmos Chem Phys* 2007; **7**: 1925–1945.

64 Shi G, Buffen AM, Ma H, *et al.* Distinguishing summertime atmospheric production of nitrate across the East Antarctic Ice Sheet. *Geochim Cosmochim Acta* 2018; **231**: 1–14.

65 Fu X, Yang X, Tan Q, *et al.* Isotopic composition of gaseous elemental mercury in the marine boundary layer of east China Sea. *J Geophys Res-Atmos* 2018; **123**: 7656–7669.

66 Ghahremaninezhad R, Norman AL, Abbatt JPD, *et al.* Biogenic, anthropogenic and sea salt sulfate size-segregated aerosols in the Arctic summer. *Atmos Chem Phys* 2016; **16**: 5191–5202.

67 Han X, Guo Q, Liu C, *et al.* Using stable isotopes to trace sources and formation processes of sulfate aerosols from Beijing, China. *Sci Rep* 2016; **6**: 29958.

68 Huang Q, Chen J, Huang W, *et al.* Diel variation in mercury stable isotope ratios records photoreduction of $PM_{2.5}$-bound mercury. *Atmos Chem Phys* 2019; **19**: 315–325.

69 Gustin MS, Amos HM, Huang J, *et al.* Measuring and modeling mercury in the atmosphere: a critical review. *Atmos Chem Phys* 2015; **15**: 5697–5713.

70 Lyman SN, Cheng I, Gratz LE, *et al.* An updated review of atmospheric mercury. *Sci Total Environ* 2020; **707**: 135575.

71 Shi G, Li Y, Jiang S, *et al.* Large-scale spatial variability of major ions in the atmospheric wet deposition along the China-Antarctica transect (31°N–69°S). *Tellus B-Chem Phys Meteorol* 2012; **64**: 17134.

72 Huang Q, Liu YL, Chen JB, *et al.* An improved dual-stage protocol to pre-concentrate mercury from airborne particles for precise isotopic measurement. *J Anal At Spectrom* 2015; **30**: 957–966.

73 Thode HG, Monster J, Dunford HB. Sulphur isotope geochemistry. *Geochim Cosmochim Acta* 1961; **25**: 159–174.

74 Defouilloy C, Cartigny P, Assayag N, *et al.* High-precision sulfur isotope composition of enstatite meteorites and implications of the formation and evolution of their parent bodies. *Geochim Cosmochim Acta* 2016; **172**: 393–409.

75 Labidi J, Cartigny P, Birck JL, *et al.* Determination of multiple sulfur isotopes in glasses: a reappraisal of the MORB δ^{34}S. *Chem Geol* 2012; **334**: 189–198.

76 Au Yang D, Landais G, Assayag N, *et al.* Improved analysis of micro- and nanomole-scale sulfur multi-isotope compositions by gas source isotope ratio mass spectrometry. *Rapid Commun Mass Spectrom* 2016; **30**: 897–907.

77 Sun R, Enrico M, Heimbürger LE, *et al.* A double-stage tube furnace—acid-trapping protocol for the pre-concentration of mercury from solid samples for isotopic analysis. *Anal Bioanal Chem* 2013; **405**: 6771–6781.

78 Yin R, Krabbenhoft DP, Bergquist BA, *et al.* Effects of mercury and thallium concentrations on high precision determination of mercury isotopic composition by Neptune Plus multiple collector inductively coupled plasma mass spectrometry. *J Anal At Spectrom* 2016; **31**: 2060–2068.

79 Blum JD, Bergquist BA. Reporting of variations in the natural isotopic composition of mercury. *Anal Bioanal Chem* 2007; **388**: 353–359.

80 Geng H, Yin R, Li X. An optimized protocol for high precision measurement of Hg isotopic compositions in samples with low concentrations of Hg using MC-ICP-MS. *J Anal At Spectrom* 2018; **33**: 1932–1940.

81 Wang Z, Chen J, Feng X, *et al.* Mass-dependent and mass-independent fractionation of mercury isotopes in precipitation from Guiyang, SW China. *Comptes Rendus Geosci* 2015; **347**: 358–367.

82 Yuan S, Chen J, Cai H, *et al.* Sequential samples reveal significant variation of mercury isotope ratios during single rainfall events. *Sci Total Environ* 2018; **624**: 133–144.

83 Zhang Y, Chen J, Zheng W, *et al.* Mercury isotope compositions in large anthropogenically impacted Pearl River, South

China. *Ecotoxicol Environ Saf* 2020; **191**: 110229.

84 Chen J, Hintelmann H, Zheng W, *et al.* Isotopic evidence for distinct sources of mercury in lake waters and sediments. *Chem Geol* 2016; **426**: 33–44.

85 National Geophysical Data Center. 2-minute Gridded Global Relief Data (ETOPO2) v2. National Geophysical Data Center, NOAA. 2006.

86 Goudie A, Middleton N J. Desert Dust in the Global System. Berlin Heidelberg: Springer-Verlag, 2006.

87 Zhang Y, Jacob DJ, Horowitz HM, *et al.* Observed decrease in atmospheric mercury explained by global decline in anthropogenic emissions. *Proc Natl Acad Sci USA* 2016; **113**: 526–531.

88 Selin NE, Jacob DJ, Yantosca RM, *et al.* Global 3-D land-ocean-atmosphere model for mercury: present-day versus preindustrial cycles and anthropogenic enrichment factors for deposition. *Glob Biogeochem Cycle* 2008; **22**: GB2011.

89 Zhang Y, Jacob DJ, Dutkiewicz S, *et al.* Biogeochemical drivers of the fate of riverine mercury discharged to the global and Arctic oceans. *Glob Biogeochem Cycle* 2015; **29**: 854–864.

90 Amos HM, Jacob DJ, Holmes CD, *et al.* Gas-particle partitioning of atmospheric Hg(II) and its effect on global mercury deposition. *Atmos Chem Phys* 2012; **12**: 591–603.